

Recalibration of the k - ω - γ Transition Model in UNITS and Application to Transition Prediction of Blunt Cones

*Muchen Yang**, *Guangxing Wang***, *Zhixiang Xiao***, *Song Fu***
School of Aerospace Engineering, Tsinghua University
Beijing, 100084, P.R.China

Abstract

The k - ω - γ transition model was implemented in the in-house structured CFD solver UNITS and the first-mode, second-mode and crossflow-mode timescale were recalibrated using test cases including the incompressible and hypersonic flows over a flat plate, and an infinite sweep-wing configuration at low speed. Finally, based on the results of the linear stability theory, a modification to the second-mode timescale was proposed to capture the nose bluntness effects on the transition of straight cones and the flow transition of cones with several different nose bluntness was investigated. Compared with the original k - ω - γ model, the improved model accurately captures the nose bluntness effects and shows good agreement with experiment.

1. Introduction

The prediction of laminar-turbulent transition of boundary layer is one of the key aspects related to the design of hypersonic vehicles. The transition has a significant impact on aerodynamic drag, heating, and vehicle operation because friction and heat transfer increase rapidly and reach maximum values in transition region. The nose bluntness of the vehicle has a large influence on the instability properties of the laminar boundary and hence on the transition location. Many studies related to effect of nose bluntness on transition, both experimental, theoretical and computational, have been done in recent years.

In the aspect of experiment, Stetson et al.[1] performed an experiment on an 8° half-angle cone to explore the effects of nose bluntness, angle of attack and boundary layer cooling on boundary layer transition and found that a transition reversal phenomenon appeared with increasing nose bluntness, which was also observed in Mach 10-12 experiment conducted by Softley[2]. Then, Stetson[3] conducted a series of experiments on an 8-degree half-angle, 4 inches base cone in the Air Force Research Laboratory Mach 6 High Reynolds Number facility and divided three regions of the entropy layer to reflect dominant nose-tip blunting effects based upon these studies. Marineau et al.[4] also conducted a series of experiments to research the transition phenomenon of cones with different nose bluntness.

In the numerical side, Rosenboom et al.[5] did linear stability study on three cases of blunt cones with different nose radii which covered both small and large bluntness and confirmed a monotonic downstream movement of the second-mode critical Reynolds number as the nose radius increases. Zhong[6] conducted a numerical study on the effects of nose bluntness on the receptivity to free-stream acoustic waves for hypersonic flow by comparing the results of three nose radii. Lei and Zhong[7] conducted a linear stability analysis on Stetson and Rushton's Mach 5.5 experiments[1] and found no clear evidence of the reversal phenomenon, which was inconsistent with the experiment results. Li et al.[8] performed a Mach 6 DNS computation at 1 degree AoA for a cone with $T_w/T_0 = 0.45$, $R_n = 1\text{mm}$, and $Re = 10 \times 10^6$ and found that the transition line on the cone surface showed a non-monotonic curve and the transition was delayed in the range of 20° ~30° ($\theta=0^\circ$ is the leeward section). Zhou et al.[9] modified the second-mode timescale of k - ω - γ transition model to improve the prediction accuracy of nose bluntness effects.

Different kinds of transition prediction approaches have been developed by far, such as semi-empirical e^N method, direct numerical simulation (DNS), large eddy simulation (LES), and transition models based on Reynolds averaged Navier–Stokes (RANS) equations. From engineering point of view, modeling the flow transition based on the RANS approach is still the best accessible way and has received significant research attention in recent years. Many transition models have been developed and the intermittency factor γ , defined as the probability of the flow being turbulent in a given spatial point, was commonly adopted to describe and activate the transition process[10][11][12][13]. However, non-local variables are used in these models, such as the boundary layer momentum thickness, which is numerically expensive and gives rise to seriously implementation difficulties in modern CFD solvers. Langtry and Menter[14][15][16] proposed a correlation-based γ - $Re_{\theta t}$ model, which was strictly based on local variables. This model has been tested in a number of cases and showed a good agreement with experiment results. However, original γ - $Re_{\theta t}$

model was designed and validated in subsonic or transonic regimes and only predicts two-dimensional transition phenomena such as transition due to Tollmien–Schlichting instabilities and separation-induced transition. Thus, transition due to crossflow instabilities in three-dimensional boundary layer or second-mode disturbances in hypersonic boundary layer were not considered in original $\gamma-Re_{\theta t}$ model. Khalil and Frauholz[17] tested the performance of $\gamma-Re_{\theta t}$ model in hypersonic regime. Krause[18] and You[19] made some modifications of the original $\gamma-Re_{\theta t}$ model to give a better performance in the prediction of hypersonic boundary layer transition. However, suffering from the lack of physical mechanism of transition, their modifications still need further investigation. Besides, many researches have been done to extend the $\gamma-Re_{\theta t}$ model to predict transition due to crossflow instability, such as Langtry[20], Krumbein[21], Choi and Kwon[22], et al.

Based on the modeling of instability wave of Hassan[23], Wang and Fu[24] proposed a $k-\omega-\gamma$ transition model, which is capable of predicting flow transition in a wide range of Mach numbers and is strictly based on local variables by introducing a length scale normal to the wall. Wang then extended this model to capture the bypass and separation-induced transition effects common in turbomachinery flows[25] and established a new formula to convert measured free-stream noise level to FSTI (freestream turbulence intensity) that is more adopted by engineering transition approaches[26]. Zhou et al.[9] improved the original $k-\omega-\gamma$ model by reformulating the γ transport equation to retain the physical information contained in the empirical correlations and modifying the timescale of the second-mode to improve the prediction accuracy of nose bluntness effects.

The first objective of this article is to recalibrate the original $k-\omega-\gamma$ transition model. Wang and Fu developed this model in an incompressible code, which is based on SIMPLE approach. Although they adopt AUSM+ method to simulate hypersonic flow, it is difficult to simulate flow over complex geometries. The computations in this paper are based on an in-house compressible solver, unsteady Navier-Stokes equation solver(UNITs), in a cell-centered finite-volume formulation. The convective fluxes are discretized by Roe scheme, and a modified fully implicit low-upper symmetric Gauss-Seidel method with Newton-like sub-iteration in pseudo time is taken as the time marching method. Due to the differences in the numerical methods, recalibration of the coefficients in original $k-\omega-\gamma$ model is necessary. The second objective is to improve the $k-\omega-\gamma$ transition model through modification of the second-mode timescale to reflect the effects of nose bluntness on transition. Zhou's modification[9] needs a prior knowledge of the geometric bluntness, so it is difficult to apply to irregular geometry and conditions with non-zero angle of attack. Our modification is based on the results of linear stability theory, which has a stable foundation of physical mechanism.

This article is organized as follows. Section 2 gives descriptions of original and improved $k-\omega-\gamma$ transition model. Section 3 gives computational results, including recalibration of original model on flat plates and an infinite sweeping configuration, calibration and application of improved model on transition prediction of straight cones with different nose bluntness. Conclusions are given in Section 4.

2. Numerical Method

2.1 Original $k-\omega-\gamma$ transition model

The original version of $k-\omega-\gamma$ transition model was proposed by Wang and Fu for hypersonic boundary layer transition[24]. This model is based on the SST model and it consists of three transport equations for the turbulent kinetic energy k , the specific turbulent dissipation rate ω and the intermittency factor γ :

$$\frac{\partial(\rho k)}{\partial t} + \frac{\partial(\rho u_j k)}{\partial x_j} = P_k + D_k - \varepsilon_k \quad (1)$$

$$\frac{\partial(\rho \omega)}{\partial t} + \frac{\partial(\rho u_j \omega)}{\partial x_j} = P_\omega + D_\omega - \varepsilon_\omega + Cd_\omega \quad (2)$$

$$\frac{\partial(\rho \gamma)}{\partial t} + \frac{\partial(\rho u_j \gamma)}{\partial x_j} = P_\gamma + D_\gamma - \varepsilon_\gamma \quad (3)$$

In the fully turbulent region, the present transition model returns to the original SST model. The effective viscosity plays a dominant role when predicting the flow transition in the above transport equations. It will switch to the conventional eddy viscosity μ_t when the flow becomes fully turbulent after the transition. Before the transition, μ_{eff} can reflect the effective viscosity caused by the laminar or non-turbulent fluctuations in the flow. A simple but effective relation serving these purposes is :

$$\mu_{eff} = (1 - \gamma) \mu_{nt} + \gamma \mu_t \quad (4)$$

where variable γ is the intermittency factor, which can bridge the non-turbulent and turbulent contributions. When γ is 0, the flow is laminar. When it is equal to 1, the flow becomes fully turbulent. When it is between 0 and 1, the flow is in the process of transition.

The non-turbulent viscosity is modeled as

$$\mu_{nt} = C_\mu \rho k \tau_{nt} \quad (5)$$

where C_μ is the model constant, k is the total fluctuating kinetic energy and τ_{nt} represents a characteristic timescale in the flow transition, which reflects the frequency character of the wave. Modeling of the timescale becomes the crucial aspect in the non-turbulent viscosity coefficient μ_{nt} . The specific modeling formulas for the first-mode, second-mode and crossflow-mode timescales are shown as equations (6)~(8). The detailed information can be found in reference[24].

$$\tau_{nt1} = C_2 \cdot \zeta_{eff}^{1.5} / [(2E_u)^{0.5} \nu]^{0.5} \quad (6)$$

$$\tau_{nt2} = C_3 \cdot 2\zeta_{eff} / U(y_s) \quad (7)$$

$$\tau_{cross} = C_7 \cdot \left(4 \frac{\zeta_{eff}}{U_e} \right) \times \left\{ 1 - \exp \left[1.0 - C_8 \left(\zeta_{eff} \frac{U_e}{\nu_e} - 44 \right)^2 \right] \right\} \times (W/U_e)^{C_9} \quad (8)$$

The overall timescale is the sum of the above three timescales:

$$\tau_{nt} = \tau_{nt1} + \tau_{nt2} + \tau_{cross} \quad (9)$$

A length scale ζ normal to the wall is introduced in present transition model to avoid the appearance of boundary layer thickness, which is regarded as non-local variable.

$$\zeta = d^2 \Omega / (2E_u)^{0.5} \quad (10)$$

where d is the distance to the nearest wall; Ω is the absolute value of the mean vortices; and E_u stands for the kinetic energy of the mean flow related to the wall. Derivation of this transition length scale comes from the relationship firstly used by Wilcox[27] that

$$\text{Re}_{\nu, \max} = \left(\frac{\rho d^2 \Omega}{\mu} \right)_{\max} = 2.193 \left(\frac{\rho U \theta}{\mu} \right) = 2.193 \text{Re}_\theta \quad (11)$$

$$\zeta_{eff} = \min(C_1 \zeta, l_T) \quad (12)$$

$$l_T = \frac{k^{0.5}}{\beta^* \omega} \quad (13)$$

The source terms of γ equation are defined as follows:

$$P_\gamma = C_4 f(Tu) \rho F_{onset} [-\ln(1 - \gamma)]^{0.5} \left(1 + C_5 \frac{k^{0.5}}{(2E_u)^{0.5}} \right) \frac{d}{\nu} |\nabla E_u| \quad (14)$$

$$\varepsilon_\gamma = \gamma P_\gamma \quad (15)$$

where the transition onset function F_{onset} and turbulence level function $f(Tu)$ [26] is defined as :

$$F_{onset} = 1.0 - \exp \left(-C_6 \frac{\zeta_{eff} k^{0.5} |\nabla k|}{\nu |\nabla E_u|} \right) \quad (16)$$

$$f(Tu) = \sqrt{1.25 \times 10^{-11} (Tu)^{7/4}} \quad (17)$$

The $C_1 \sim C_9$ are the model constants and the values after recalibration are listed in Table 1.

2.2 Improved $k-\omega-\gamma$ transition model

For hypersonic flow over spherical cones of small nose radii, it has been experimentally observed and theoretically explained that the nose bluntness effect leads to a delay of boundary-layer transition. In contrast, this trend reverses when the nose radii are larger than some critical values. The following Fig. 1 shows the relationship between the transition Reynolds number $((Re_s)_{TR})$ and free stream Reynolds numbers based on nose radii (Re_n) . There is a clear transition reversal as Re_n increases, with approximately 2×10^5 as the dividing line.

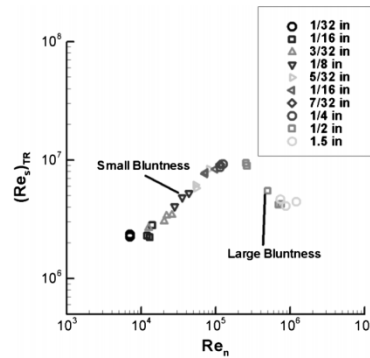


Figure 1 $(Re_s)_{TR}$ vs Re_n reported by Stetson and Rushton[1]

Zhong[7] conducted a linear stability analysis on Stetson and Rushton's[1] Mach 5.5 experiments in which the transition reversal is observed. In the research, he found that as the nose becomes blunter, the local Reynolds number within the boundary layer is substantially reduced, which causes a delay in the onset of second-mode instabilities and moves the transition location further downstream. Fig. 2 shows the second-mode neutral stability curves for three different nose bluntness cones.

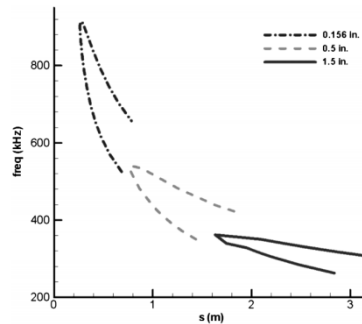


Figure 2 Second-mode neutral stability curve for cones with three different nose radii[6]

Therefore, Zhou [9] made a modification to the second-mode timescale in the “small bluntness” region to improve the prediction accuracy of transition for different nose bluntness cones. The modification of the second-mode timescale is defined as follows:

$$\tau_{nt2,Zhou} = \begin{cases} \tau_{nt2}, & R_n = R_0 \\ 0.559 \frac{R_1}{R_n} \tau_{nt2}, & R_n > R_0 \end{cases} \quad (18)$$

where $R_0 = 0.00254 \text{ mm}$ is the base nose bluntness. The modification obtained a good result for different nose bluntness cones at 0 degree angle of attack. However, the modification depends on the geometric bluntness so it is difficult to apply to irregular geometry and conditions with non-zero angle of attack.

Zhong[7] also pointed out that the local unit Reynolds number within the boundary layer is substantially reduced as the nose becomes blunter. We hope an improved transition model delay the development of second-mode instability wave for blunt cones and return to original model for sharp cones. Thus, by taking the local unit Reynolds number into account, we proposed a new modification to second-mode timescale as follows :

$$\tau_{nt2,new} = C_{3,new} \left(\frac{Re_{local}}{Re_{\infty}} \right)^{C_0} \tau_{nt2} \quad (19)$$

where Re_{local} and Re_{∞} are the local unit Reynolds number and the freestream unit Reynolds number, respectively. $C_{3,new}$ and C_0 are model constants which need to be calibrated. The purpose of modification is to delay the development of the second-mode timescale for blunt cones.

Table 1 Model constants

Model constants	C_0	C_1	C_2	C_3	C_4	C_5	C_6	C_7	C_8	C_9
Original		7000	0.1	3.2	350.0	0.07	1.2	4.8	0.001	0.5
Improved	0.5	7000	0.1	36.0	350.0	0.07	1.2	4.8	0.001	0.5

3. Results and discussion

3.1 Recalibration of original $k-\omega-\gamma$ transition model

a. Low speed flat plate

The flat plate experiment of Schubauer and Klebanoff[28] is investigated in the simulation in order to validate the capability of present model to predict the low speed flow transition due to Tollmien–Schlichting instabilities. A grid-dependency test was performed using three grids to examine the effect of grid resolution, as summarized in Table 2, and the fine grid is shown in Fig. 3. The computational conditions are shown in Table 3.

Table 2 Computational grids for flat plate

Grid	Coarse	Medium	Fine
Number of streamwise nodes of flat plate	401	567	801
Growth rate in boundary layer	1.15	1.1	1.05
Surface y^+ values in turbulent region	0.6	0.45	0.3
Total number of nodes	451×102	637×143	901×202

Table 3 Computational conditions of low speed flat plate

Case	Ma	$Re(/m)$	$T(K)$	$T_w(K)$	$AOA(^{\circ})$	$FSTI(\%)$
Flat plate	0.147	3.3×10^6	293	Adiabatic	0	0.18

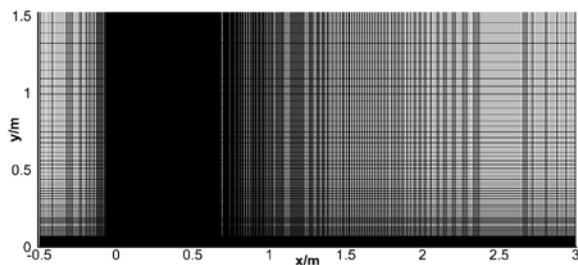


Figure 3 Computational grid for flat plate

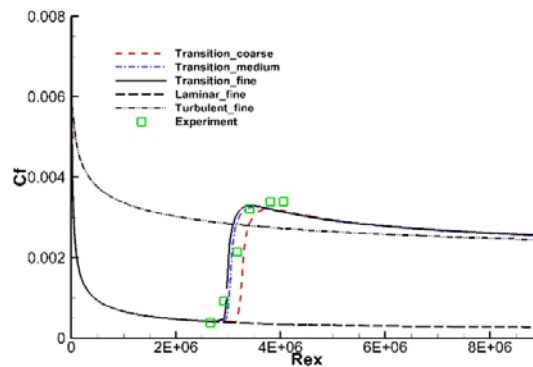
Figure 4 Skin friction coefficient (C_f)

Figure 4 presents distributions of skin friction coefficient along streamwise direction of experiment and numerical simulation (laminar, transition model, turbulence model). There is a slight difference in the transition simulation among the grids and the finer two grids almost yield the identical results. The results of the transition model agree well with the experiment.

b. Hypersonic flat plate

The second-mode disturbance timescale, which is dominant in high-Mach flow transition, was calibrated using hypersonic flat-plate. The experiment was carried out at $M = 6.2$ in a shock-tunnel facility by Mee[29]. The computational conditions are shown in Table 4. The computational grids are the same with low speed flat plate. Fig. 5 presents the distributions of Stanton number of the numerical simulation and experiment. It is found that the flow transition profile is well captured with the present model.

Case	Ma	$Re(/m)$	$T(K)$	$T_w(K)$	$AOA(^{\circ})$	$FSTI (%)$
Flat plate	6.2	2.6×10^6	690.0	690	0	0.32

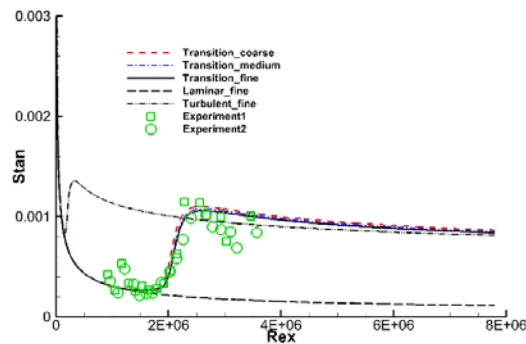


Figure 5 Comparison of Stanton number

c. Infinite swept NLF(2)-0415 wing

To validate the performance of present model in the prediction of crossflow instability induced transition, the flow past infinite NLF(2)-0415 wing with a sweep angle of 45 degree[30] was investigated, and the results were compared with those of the experiment. The measurements were made at an angle of attack of -4 degrees with Reynolds number based on freestream velocity and chord length ranging from 1.93×10^6 to 3.73×10^6 . A grid-dependency test was performed using three grids to examine the effect of grid resolution, as summarized in Table 5. The grids were clustered to the surface with an initial thickness of 1.0×10^{-5} c and a grown factor of 1.15 to capture the boundary layer flow accurately. The wing span was extended by 0.3 chord lengths, with periodic boundary condition imposed at the side boundaries to represent an infinite wing in span, as shown in Fig. 6.

Grid	Coarse	Medium	Fine
Number of nodes	1 402 908	2 632 396	4 488 036
Maximum cell size on upper surface	0.006 C	0.004 C	0.003 C

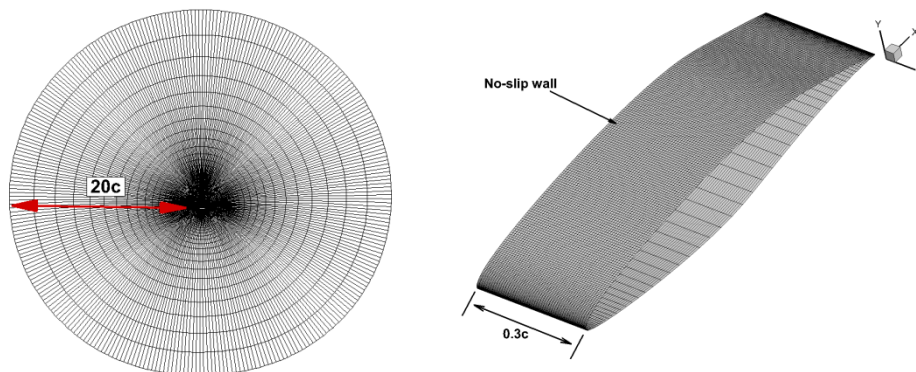


Figure 6 Computational grids of infinite swept NLF(2)-0415 wing

The distributions of surface friction coefficient along the streamwise direction on the upper surface of $Re = 3.73 \times 10^6$ are shown in Fig. 7. It is shown that the medium grid and fine grid almost yielded the identical results. However, there

was a slight difference between the coarse grid and the finer two grids. Thus, the medium grid is sufficient for accurately capturing the crossflow instability induced transition. The distribution of surface intermittency factor predicted using the medium grid is also shown in Fig. 7.

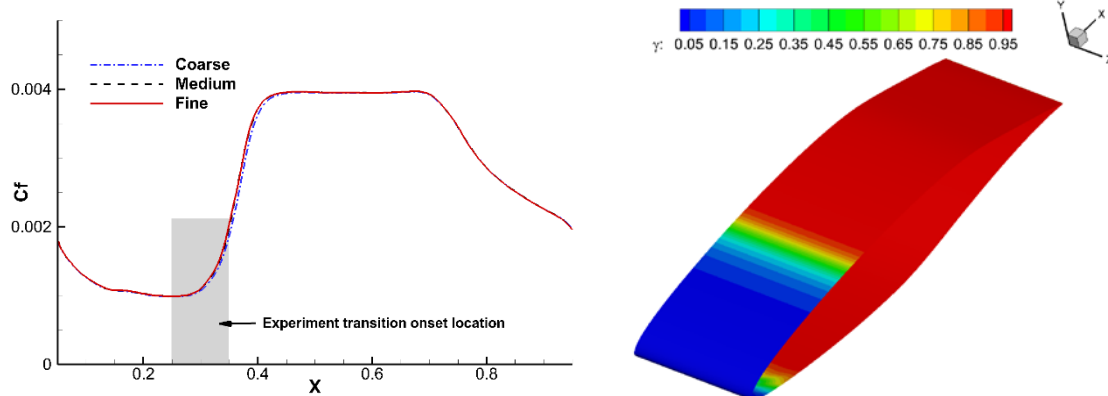


Figure 7 Distribution of surface friction coefficient and intermittency factor

The transition locations for different Reynolds number on the upper surface are shown in Fig. 8. Without taking crossflow into consideration ($C_7=0$), the transition onset locations predicted were almost identical for different Reynolds numbers, which was quite different from the experiment results. With the consideration of crossflow, the present model generally well captured the transition locations, which indicates that present model is capable of predicting transition induced by crossflow instability.

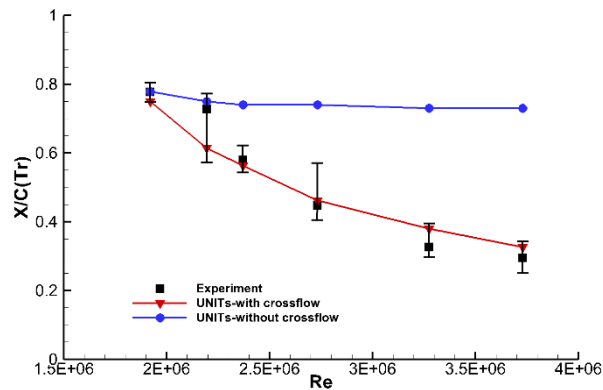


Figure 8 Transition onset location at different Reynolds number

3.2 Calibration of improved $k-\omega-\gamma$ transition model

Three different nose bluntness cones of Horvath's experiments[31] are chosen to calibrate the model constants in the improved transition model.

The cones have a length of 635 mm and a semi vertex angle of 5° , with nose bluntness of 0.00254, 0.78375 and 1.5875 mm, as shown in Fig. 9.

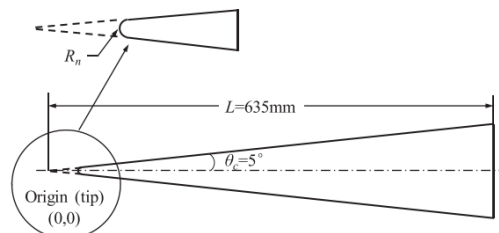
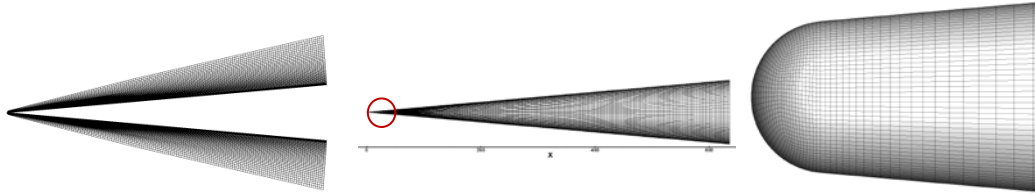


Figure 9 Schematic diagram of straight cone model[31]

Figure 10 Grids on the symmetrical plane and surface ($R_n=0.00254mm$)

Three different grids are adopted for the specific R_n to ensure convergence of the grids. The near-wall grid nodes were clustered to the wall to ensure that y^+ values were between $0 < y^+ < 1$ for all simulations. The normal growth rate was 1.05 in the boundary layer and there was almost no gradient in the circular direction for the 0° of AoA, so only the grids in the streamwise direction were refined. Computational conditions are shown in Table 6 the wall temperature T_w is 306.36 K.

Table 6 Computational conditions

$R_n(mm)$	Ma	$Re (/m)$	$T_\infty(K)$	$AOA (^\circ)$	$FSTI (\%)$	$Grid$
0.00254	6.0	2.56×10^7	63.0	0	0.34	201×91×105(Coarse)
						285×91×105(Medium)
						401×91×105(Fine)
0.79375	6.0	2.56×10^7	63.0	0	0.34	161×91×105(Coarse)
						227×91×105(Medium)
						321×91×105(Fine)
1.5875	6.0	2.56×10^7	63.0	0	0.34	145×91×105(Coarse)
						205×91×105(Medium)
						291×91×105(Fine)

a. The basic flow field

A characteristic feature of hypersonic flow over a sphere-cone configuration is that the high-pressure gas generated by the nosetip bow shock overexpands as it travels down, requiring a recompression to arrive at the "proper" pressure at some downstream location on the cone, as shown in Fig. 11.

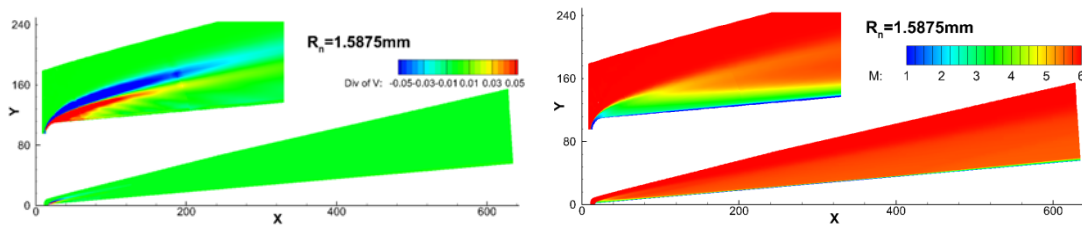


Figure 11 Divergence of velocity and Mach number

b. The influence of nose bluntness to the flow

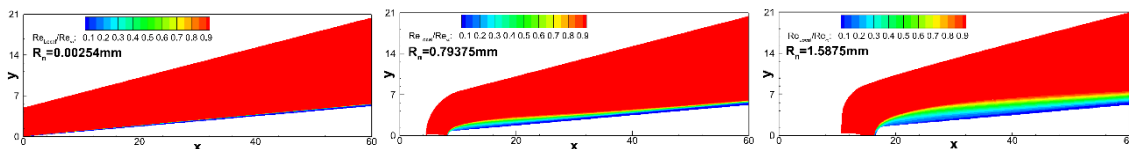


Figure 12 Contours of ratio of local unit Reynolds number to freestream unit Reynolds number

The contours of the ratio of local unit Reynolds number to freestream unit Reynolds number for three cases are shown in Fig. 12. As the nose becomes blunter, the local Reynolds number within the boundary layer is substantially reduced. This unique pattern caused a delay in the onset of second-mode instabilities and, hence, moved the transition location further downstream. This theory has been verified experimentally on small bluntness cones[3].

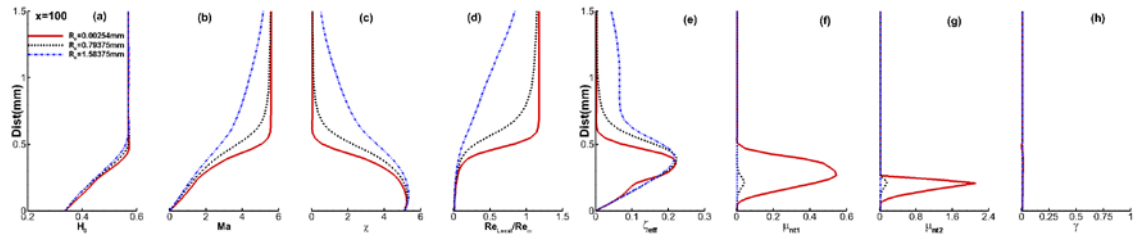


Figure 13 Profiles of flow variables along the wall normal direction at $x=100$ mm for three nose bluntness cones

In order to explore the influence of the different nose bluntness to the basic field, the mean flow variables of pre-transitional region $x=100$ mm are chosen. Fig. 13 shows several flow variables at the location $x=100$ mm for three nose bluntness cones computed by the improved transition model. Local entropy, χ is computed assuming a perfect gas as Reference[32], which is expressed as

$$\chi = \frac{\gamma_g}{\gamma_g - 1} \ln\left(\frac{T}{T_\infty}\right) - \ln\left(\frac{p}{p_\infty}\right) \quad (20)$$

The boundary layer thickness increases with increasing R_n from the profile of the total enthalpy. However, local Mach number and the ratio of local unit Reynolds number to free stream unit Reynolds number have a rapid decreasing with increasing nose bluntness. On the contrary, as shown in Fig. 13c, the entropy χ presents a rapid increasing trend as the noses get blunter. It is found that the entropy layer has a strong reduction effect on the edge Mach numbers and local Reynolds numbers[6].

In the transition model, the non-turbulent viscosity is composed of μ_{nt1} and μ_{nt2} , which reflects the contribution to effective viscosity before the transition. Since the free stream Mach number is 6.0, the second-mode dominates the transition. From Fig. 13f and Fig. 13g, μ_{nt1} and μ_{nt2} hardly develop at the position of $x=100$ mm for $R_n=1.5875$ mm cone compared with the cone $R_n=0.00254$ mm. Therefore, the transition onset moves toward the downstream direction with the nose bluntness Reynolds number increases in the region of “small bluntness”.

c. Comparison of results simulated by original and improved transition model

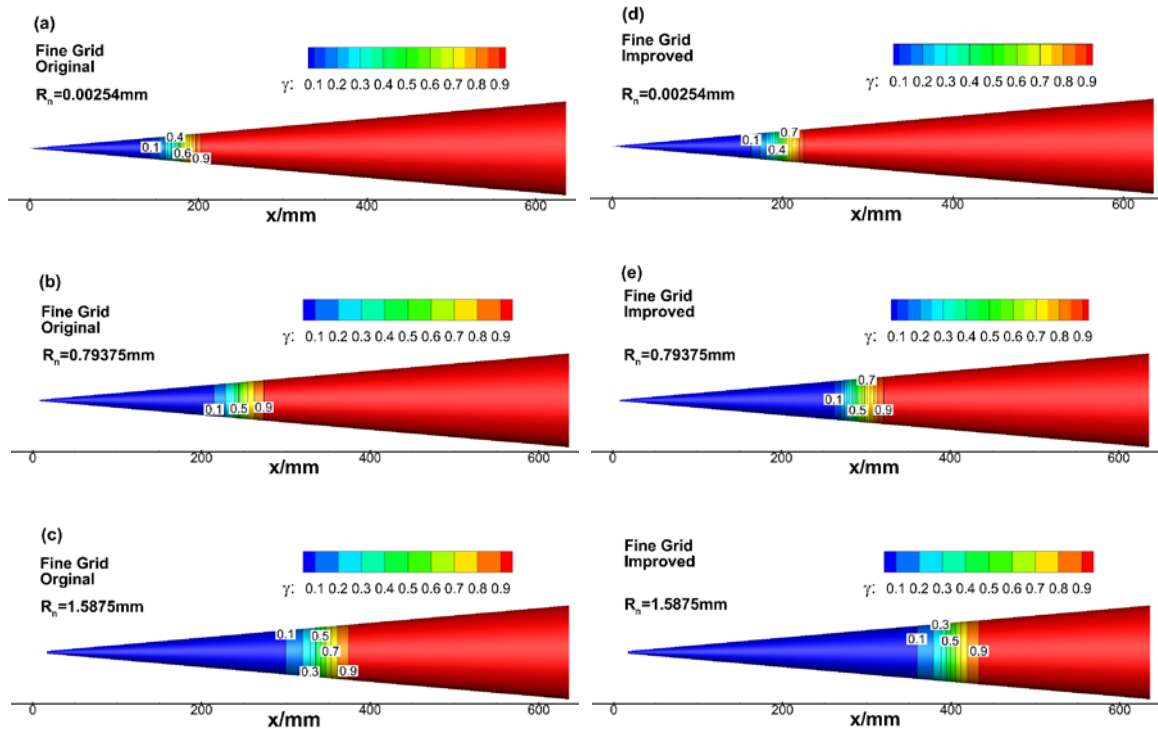


Figure 14 Intermency factor of surface with different nose bluntness

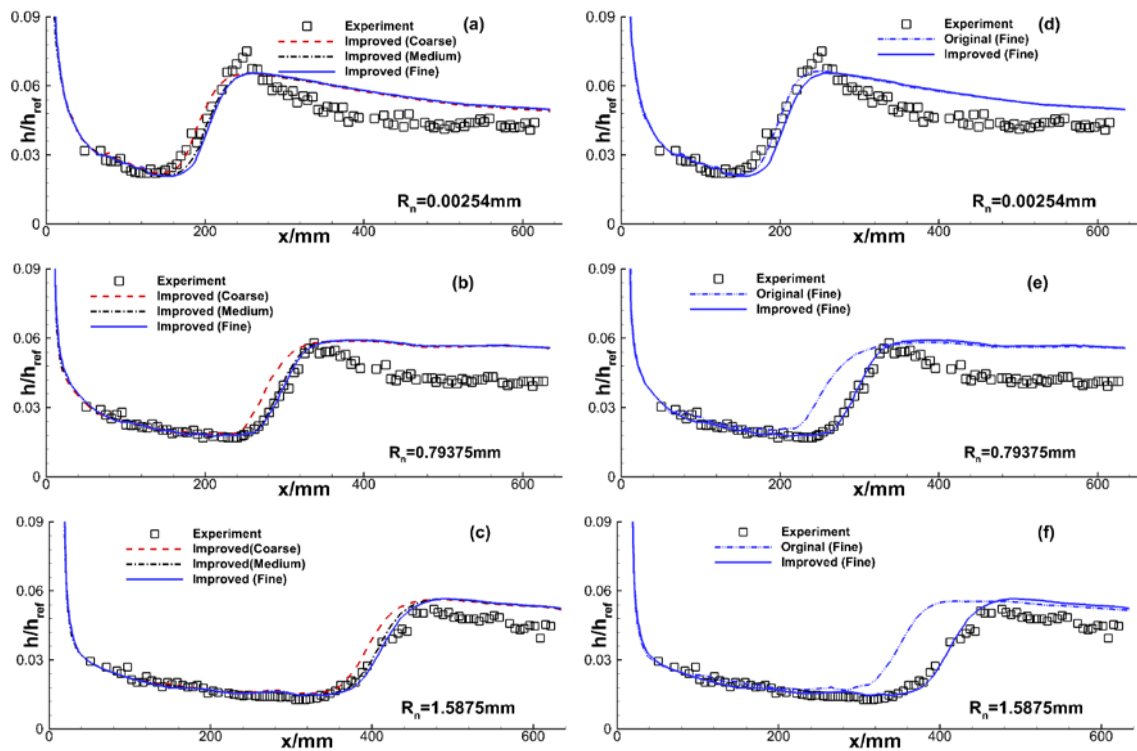
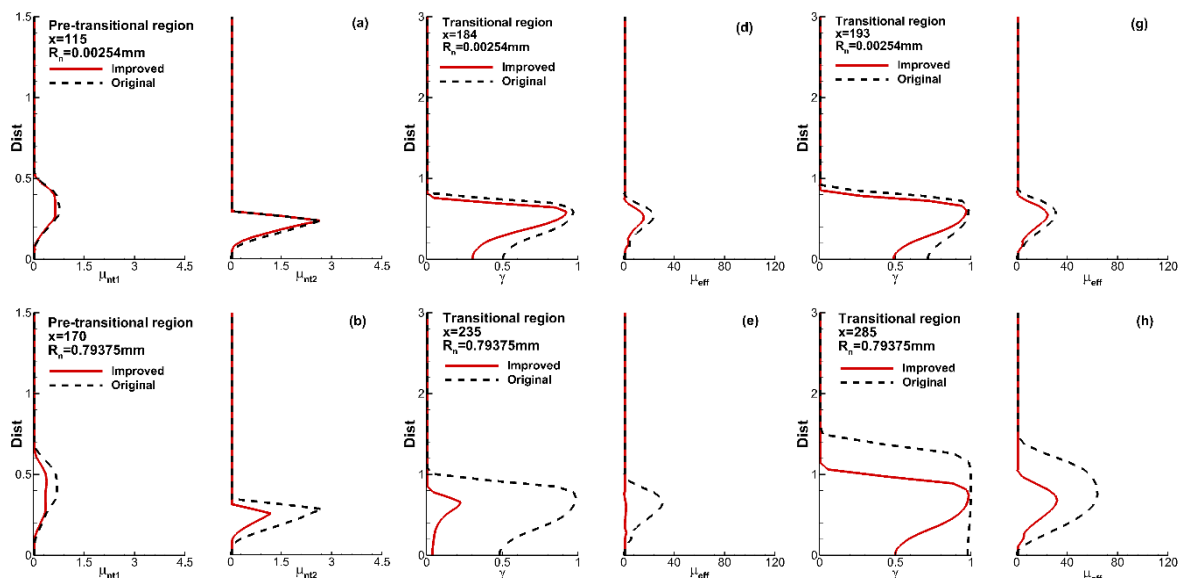


Figure 15 Comparison of h/h_{ref} distributions simulated by the original and improved transition model to the experimental results for three nose bluntness

Figure 14 and Figure 15 show the distributions of intermittency factor of the wall and h/h_{ref} along streamwise direction on different nose bluntness cones computed by original and improved transition model. The transition onset locations simulated by both original and improved transition model present a backward trend as the nose get blunter. There is a slight difference for the sharp cone ($R_n=0.00254\text{ mm}$) between the two models.

Figure 15a-c present the h/h_{ref} distributions using three different grids for each nose bluntness cone. The results show slight differences between the medium grid and fine grid, which implies grid convergence of the current numerical simulations. The original transition model presents a result which agrees well with the experiment for the sharp cone ($R_n=0.00254\text{ mm}$) and the improved model nearly returns to the original transition model for the sharp cone. However, the original model predicted forward transition locations for the blunter cones ($R_n=0.79375\text{ mm}$ and $R_n=1.5875\text{ mm}$) and the difference gets larger with the increasing nose bluntness. Compared with the original transition model, the improved transition model agrees much better with the experiment data.



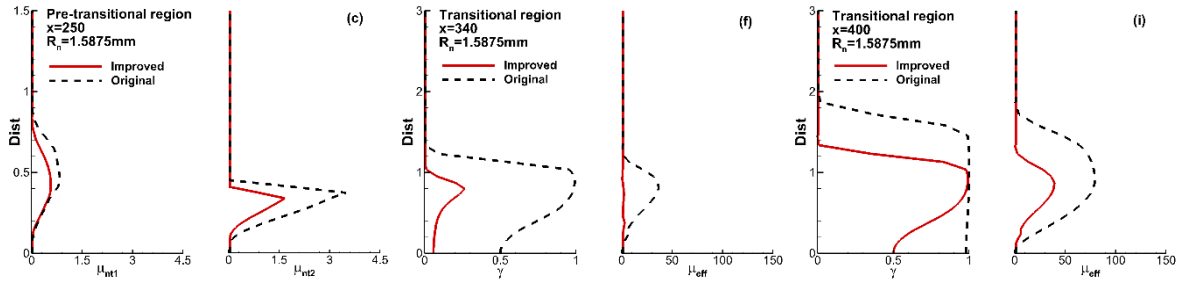


Figure 16 Comparison of flow variables in pre-transitional and transitional regions

To further analyze the differences of transition simulation between original and improved transition model, profiles of mean flow variables along the wall normal direction in the pre-transitional region and the transitional regions are chosen for each cone. We define the region where intermittency factor $\gamma < 0.01$ as pre-transitional region and the region between the pre-transitional region and fully turbulent region as transitional region. In the pre-transitional region, non-turbulent viscosity μ_{nt1} and μ_{nt2} , which reflect the contribution to effective viscosity before the transition are shown. However, in the transitional region, μ_{nt1} and μ_{nt2} are relative smaller compared with μ_{eff} , thus intermittency factor γ and the effective viscosity μ_{eff} will be the suitable variables to describe the transition process.

Figure 16a~c show μ_{nt1} and μ_{nt2} for three different nose bluntness cones in the pre-transitional region. The non-turbulent viscosity μ_{nt2} dominates the transition simulated by both transition models. For the sharp cone ($R_n = 0.00254$ mm), μ_{nt2} simulated by original transition model is slightly larger than improved model, thus the development of γ is a little faster compared with the improved model. In contrast, for the blunt cones ($R_n = 0.79375$ mm and $R_n = 1.5875$ mm), μ_{nt2} simulated by original transition model are much larger than the improved model. As a result, in region near wall, the intermittency factor γ simulated by original transition model gets approximately 0.5 while the value of γ simulated by improved transition model is below 0.1. When the intermittency factor γ simulated by improved transition model gets approximately 0.5, the counterpart of original model is approximately 1.0. The improved transition model delays the transition onset due to the modification of the second-mode timescale.

3.3 Application in transition prediction of blunt cones

In this section, several cases from Marineau's experiment[4], which was conducted in the Arnold Engineering Development Complex (AEDC) Hypervelocity Wind Tunnel 9, were chosen to validate the improved transition model. The $Re_{\infty N}$ is 2.28×10^3 for the sharp one, which has a nose radius of 0.152 mm, and 8.64×10^4 and 1.52×10^5 for the blunt one, which has a nose radius of 5.08 mm. Details about the computation setup are shown in Table 7. S_T denotes the transition onset location in the experiment, and ΔS_T is the uncertainty.

In Tunnel 9, noise at Mach 10 decreases with unit Reynolds number according to the equation in Reference[33].

$$p'_{RMS} / \bar{p} = -0.0065 \ln(Re / ft) + 0.1331 \quad (21)$$

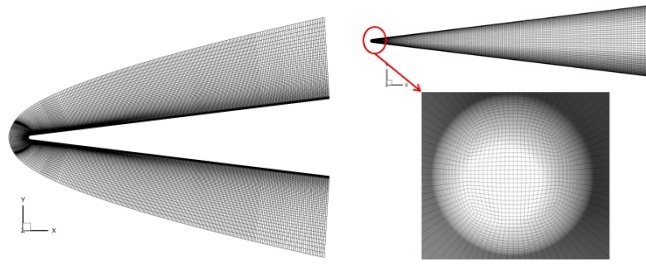
The relationship between the free stream turbulence intensity ($FSTI$) and the pressure fluctuations (PL) is as follows:

$$FSTI = PL / (\gamma_s Ma) \quad (22)$$

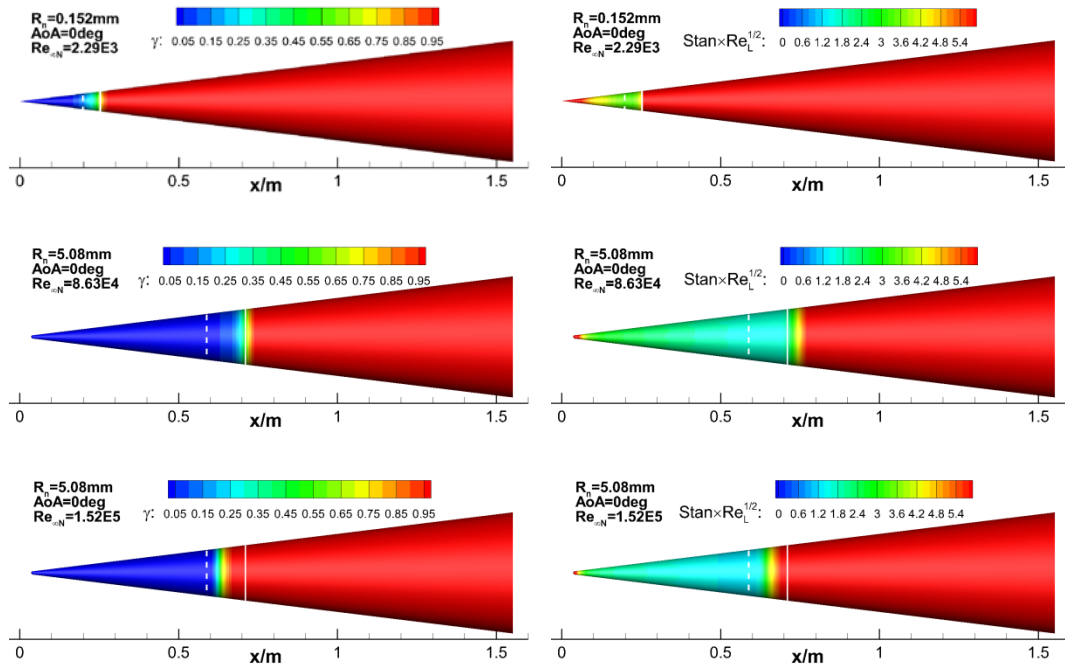
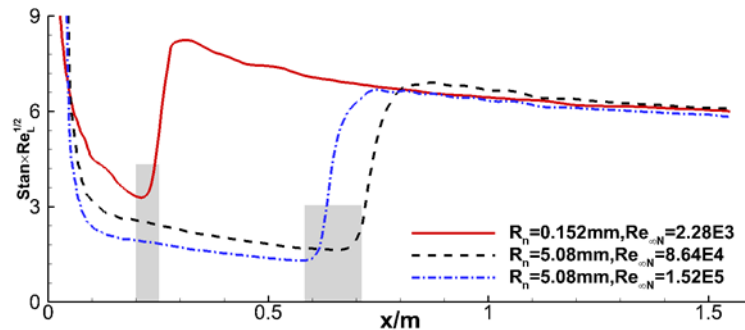
The wall to stagnation point temperature ratio (T_w/T_0) was approximately 0.3.

Table 7 Computation setup

R_n/mm	Ma_{∞}	$Re_{\infty N}/(m)$	$T_{\infty}(K)$	$AOA(^{\circ})$	$FSTI$ (%)	$S_T(m)$	$\Delta S_T(m)$	$Grid$
0.152	9.86	2.28×10^3	53.4	0	0.242	0.254	0.0508	307×89×89
5.08	9.81	8.64×10^4	50.8	0	0.237	0.683	0.128	285×89×89
5.08	10.0	1.52×10^5	51.8	0	0.206	0.683	0.128	285×89×89

Figure 17 Computational grid ($R_n=5.08mm$)

The distributions of intermittency factor and $Stan \times Re_L^{(1/2)}$ are shown in Fig. 18, and the transition onset locations in experiment are labeled as solid lines, with dashed lines denote error band of the experiment. The transition process is generally well captured by the improved model. Fig. 19 presents the distributions of $Stan \times Re_L^{(1/2)}$ along streamwise direction, from which the transition onset location is easier to distinguish. It is found that the transition onset locations predicted by the improved model are within the error band of experiment results denoted by the transparent gray area, which shows the effectiveness of the improved model.

Figure 18 Intermittency factor and $Stan \times Re_L^{(1/2)}$ distributions on the wallFigure 19 Distributions of $Stan \times Re_L^{(1/2)}$ on the wall along streamwise direction

4. Conclusions

The $k-\omega-\gamma$ transition model was recalibrated in the in-house structured CFD solver UNITS using several cases, through which the capability of present model to predict transition due to first-mode, second-mode, and crossflow instabilities was validated. Considering the influence of nose bluntness on the transitional process in “small bluntness”

region, a modification of second-mode timescale was proposed according to the results of linear stability theory, which has a stable foundation of physical mechanism. The delay trend of transition onset position on cones with increasing nose bluntness was accurately captured by introducing the ratio local unit Reynolds Number to free stream unit Reynolds Number in the second-mode timescale. Meanwhile, the improved transition model almost return to the original transition model for the sharp cones. The performance of the improved model in transition prediction of cones with non-zero angle of attack is ongoing and the reversal trend in even larger nose bluntness need further investigation.

Acknowledgments

The authors would like to thank the National Natural Science Foundation of China (Grant No. 11372159) and the National Key Research and Development Program of China (Grant No. 2016YFA0401200), and express our gratitude to Tsinghua National Laboratory for Information Science and Technology for computation resources.

References

- [1] Rushton, G.H. and Stetson, K.F., 1967. Shock tunnel investigation of boundary-layer transition at M equals 5.5. *AIAA Journal*, 5(5), pp.899-906.
- [2] Softley, E. J. 1968. Transition of the Hypersonic Boundary Layer on a Cone: Part II - Experiments at Mach 10 and More on Blunt Cone Transition, in GE Space Science Lab, R68SD14.
- [3] Stetson, K.F., 1983, July. Noretip bluntness effects on cone frustum boundary layer transition in hypersonic flow. In *16th Fluid and Plasmadynamics Conference* (p. 1763).
- [4] Marineau, E.C., Moraru, G.C., Lewis, D.R., Norris, J.D., Lafferty, J.F., Wagnild, R.M. and Smith, J.A., 2014. Mach 10 Boundary Layer Transition Experiments on Sharp and Blunted Cones. In *19th AIAA International Space Planes and Hypersonic Systems and Technologies Conference* (p. 3108).
- [5] Rosenboom, I., Hein, S. and Dallmann, U., 1999, June. Influence of nose bluntness on boundary-layer instabilities in hypersonic cone flows. In *30th Fluid Dynamics Conference* (p. 3591).
- [6] Zhong, X., 2004. Numerical Simulation and Experimental Comparison of Hypersonic Boundary Layer Instability over a Blunt Cone. In *34th AIAA Fluid Dynamics Conference and Exhibit* (p. 2244).
- [7] Lei, J. and Zhong, X., 2012. Linear stability analysis of nose bluntness effects on hypersonic boundary layer transition. *Journal of Spacecraft and Rockets*, 49(1), pp.24-37.
- [8] Li, X., Fu, D. and Ma, Y., 2010. Direct numerical simulation of hypersonic boundary layer transition over a blunt cone with a small angle of attack. *Physics of Fluids*, 22(2), p.025105.
- [9] Zhou, L., Yan, C., Hao, Z.H. and Du, R.F., 2016. Improved $k-\omega-\gamma$ model for hypersonic boundary layer transition prediction. *International Journal of Heat and Mass Transfer*, 94, pp.380-389.
- [10] Steelant, J. and Dick, E., 1996. Modelling of bypass transition with conditioned Navier–Stokes equations coupled to an intermittency transport equation. *International journal for numerical methods in fluids*, 23(3), pp.193-220.
- [11] Cho, J.R. and Chung, M.K., 1992. A $K-\epsilon-\gamma$ equation turbulence model. *Journal of Fluid Mechanics*, 237, pp.301-322.
- [12] Suzen, Y.B. and Huang, P.G., 1999. *Modeling of flow transition using an intermittency transport equation* (Vol. 209313). National Aeronautics and Space Administration, Glenn Research Center.
- [13] Suzen, Y.B., Huang, P.G., Hultgren, L.S. and Ashpis, D.E., 2003. Predictions of separated and transitional boundary layers under low-pressure turbine airfoil conditions using an intermittency transport equation. *Journal of Turbomachinery*, 125(3), pp.455-464.
- [14] Menter, F.R., Langtry, R.B., Likki, S.R., Suzen, Y.B., Huang, P.G. and Völker, S., 2006. A correlation-based transition model using local variables—Part I: model formulation. *Journal of turbomachinery*, 128(3), pp.413-422.
- [15] Langtry, R.B., Menter, F.R., Likki, S.R., Suzen, Y.B., Huang, P.G. and Völker, S., 2006. A correlation-based transition model using local variables—part II: test cases and industrial applications. *Journal of Turbomachinery*, 128(3), pp.423-434.
- [16] Langtry, R.B. and Menter, F.R., 2009. Correlation-based transition modeling for unstructured parallelized computational fluid dynamics codes. *AIAA journal*, 47(12), pp.2894-2906.
- [17] Frauholz, S., Reinartz, B.U., Müller, S. and Behr, M., 2015. Transition Prediction for Scramjets Using γ -R e₀ t Model Coupled to Two Turbulence Models. *Journal of Propulsion and Power*, 31(5), pp.1404-1422.
- [18] Krause, M., Behr, M. and Ballmann, J., 2008. Modeling of transition effects in hypersonic intake flows using a correlation-based intermittency model. In *15th AIAA International Space Planes and Hypersonic Systems and Technologies Conference* (p. 2598).

- [19] You, Y., Luedeke, H., Eggers, T. and Hannemann, K., 2012. Application of the γ -Reot Transition Model in High Speed Flows. In *18th AIAA/3AF International Space Planes and Hypersonic Systems and Technologies Conference* (p. 5972).
- [20] Langtry, R., 2015. Extending the Gamma-Rethetat Correlation based Transition Model for Crossflow Effects. In *45th AIAA Fluid Dynamics Conference* (p. 2474).
- [21] Grabe, C. and Krumbein, A., 2013. Correlation-based transition transport modeling for three-dimensional aerodynamic configurations. *Journal of Aircraft*, 50(5), pp.1533-1539.
- [22] Choi, J.H. and Kwon, O.J., 2015. Enhancement of a correlation-based transition turbulence model for simulating crossflow instability. *AIAA Journal*, 53(10), pp.3063-3072.
- [23] Warren, E.S., Harris, J.E. and Hassan, H.A., 1995. Transition model for high-speed flow. *AIAA journal*, 33(8), pp.1391-1397.
- [24] Fu, S. and Wang, L., 2013. RANS modeling of high-speed aerodynamic flow transition with consideration of stability theory. *Progress in Aerospace Sciences*, 58, pp.36-59.
- [25] Wang, L., Fu, S., Carnarius, A., Mockett, C. and Thiele, F., 2012. A modular RANS approach for modelling laminar-turbulent transition in turbomachinery flows. *International journal of heat and fluid flow*, 34, pp.62-69.
- [26] Wang, L., Xiao, L. and Fu, S., 2016. A modular RANS approach for modeling hypersonic flow transition on a scramjet-forebody configuration. *Aerospace Science and Technology*, 56, pp.112-124.
- [27] Wilcox, D.C., 1975. Turbulence-model transition predictions. *AIAA Journal*, 13(2), pp.241-243.
- [28] Schubauer, G. and Klebanoff, P., 1955, Contributions on the Mechanics of Boundary Layer Transition, NACA TN , Vol. 3489.
- [29] Mee, D.J., 2002. Boundary-layer transition measurements in hypervelocity flows in a shock tunnel. *AIAA journal*, 40(8), pp.1542-1548.
- [30] J.Ray Dagenhart, William S. Saric. 1999. Crossflow Stability and Transition Experiments in Swept-Wing Flow. Technical Report.
- [31] Horvath, T., Berry, S., Hollis, B., Singer, B. and Chang, C.L., 2002, January. Boundary layer transition on slender cones in conventional and low disturbance Mach 6 wind tunnels. In *32nd AIAA Fluid Dynamics Conference and Exhibit* (p. 2743).
- [32] Malik, M., Spall, R. and Chang, C.L., 1990, January. Effect of nose bluntness on boundary layer stability and transition. In *28th Aerospace Sciences Meeting* (p. 112).
- [33] Lafferty, J. and Norris, J., 2007. Measurements of Fluctuating Pitot Pressure," Tunnel Noise," in the AEDC Hypervelocity Wind Tunnel No. 9. In *2007 US Air Force T&E Days* (p. 1678).